ELSEVIER

Surface Science 447 (2000) 187–200

surface science

www.elsevier.nl/locate/susc

Electrochemical copper deposition on Au(100): a combined in situ STM and in situ surface X-ray diffraction study

R.J. Randler [a], D.M. Kolb [a,*], B.M. Ocko [b], I.K. Robinson [c]

[a] *Abteilung Elektrochemie, Universität Ulm, 89069 Ulm, Germany*
[b] *Department of Physics, Brookhaven National Laboratory, Upton, NY 11973, USA*
[c] *Department of Physics, University of Illinois, Urbana, IL 61801, USA*

Received 13 April 1999; accepted for publication 8 November 1999

Abstract

The electrochemical deposition of copper onto Au(100) has been investigated using in situ scanning tunneling microscopy (STM) and in situ surface X-ray scattering (SXS). Copper deposition from sulfuric acid solutions starts at potentials positive of the reversible Nernst potential, where a pseudomorphic (1×1) copper monolayer forms. Negative of the Nernst potential, STM measurements have revealed that bulk copper nucleates at the surface defects, step edges or island rims of the gold substrate. A bilayer of copper is formed on top of the underlying copper monolayer and further growth proceeds in a layer-by-layer fashion. Atomic resolution STM images have shown that the copper film has a pseudomorphic structure for films less than or equal to 10 layers. Surface X-ray scattering measurements have confirmed the pseudomorphic arrangement and have provided a precise measure of the copper layer spacing (1.45 ± 0.02 Å), in good agreement with the value obtained from the copper–copper step height in the STM measurements. This layer spacing is much smaller than the value expected for fcc copper. The combined structural analysis leads to the conclusion of a thermodynamically stable bcc-like structure. Both the X-ray and STM results suggest alloying at the copper–gold interface.

Keywords: Alloys; Copper; Electrochemical methods; Epitaxy; Gold; Metal–metal interfaces; Scanning tunneling microscopy; Single crystal surfaces; X-ray scattering, diffraction, and reflection

1. Introduction

Experimentally, for a wide variety of heteroepitaxial systems, the first layer (in rare cases the first few layers) grows pseudomorphically onto the substrate, despite the adverse effects of strain [1–4]. The stress due to the crystallographic misfit limits the thickness of such a pseudomorphic film usually to 1 monolayer (ML), or to a few monolayers if the lattice constants are sufficiently similar. According to the classical van der Merwe model of metal-on-metal epitaxy [5], the elastic strain energy of the film increases with film thickness. At a critical thickness the pseudomorphic growth stops, and the layer usually continues to grow with its own preferred structure with misfit dislocations at the interface to relieve the strain. Such dislocations can act as nucleation sites for the bulk metal, which will grow as three-dimensional clusters (Stranski–Krastanov growth).

The strain can cause novel bulk phases of a metal film to grow with crystal structures different from that of the stable bulk phase. This is observed

* Corresponding author. Fax: +49-731-502-5409.
E-mail address: dieter.kolb@chemie.uni-ulm.de (D.M. Kolb)

0039-6028/00/$ - see front matter
PII: S0039-6028(99)01170-X

when a non-equilibrium crystal structure provides a much better fit to the substrate lattice than any orientation of the natural crystal structure [6,7]. The smaller stress can make the non-equilibrium structure more favorable than the natural structure, at least for a certain thickness range. For many transition and noble metals the energy difference between the fcc, hcp, and bcc structures is quite small [8], and this suggests that non-equilibrium structures may be grown up to rather thick layers, if the overlayer lattice constant matches that of the substrate. The formation of non-equilibrium structures is often seen in metal-on-metal epitaxy for the growth of an fcc metal on the (100) surface of an fcc or bcc single crystal substrate in the case that deposit and substrate exhibit different lattice constants. While the in-plane lattice constant a of the overlayer matches exactly the lattice constant of the substrate, the lattice constant c, along the surface normal, assumes a value which is determined by the Poisson ratio of the film material. This process leads to either body-centered cubic (bcc), face-centered cubic (fcc), or body-centered tetragonal (bct) structures of the film lattice, depending on the lattice constant ratio c/a. Thus, epitaxy provides access to various new constrained-tetragonal bulk structures of crystalline materials.

One example of such a non-equilibrium crystal structure is the bcc or bct lattice of copper. This lattice provides a good fit to a number of (100) substrates, and theoretical calculations show that the bcc structure is only about 20–38 meV [9,10] less stable than the natural fcc copper structure. Such bcc and bct copper films have been obtained by the pseudomorphic growth of copper on different (100) oriented fcc substrates in UHV [11–13] as well as under electrochemical conditions [14,15]. The substrates act as a template for the growth of the copper bcc phase. Egelhoff et al. [11] and Jiang et al. [12] studied the molecular beam epitaxy (MBE) of copper on a Ag(100) substrate with reflection high energy electron diffraction (RHEED), low energy electron diffraction (LEED) and X-ray photoelectron diffraction (XPD). They showed that copper grows initially in a thermodynamic stable bct modification with lattice constants $a=2.88$ Å and $c=3.10$ Å, before it changes gradually to fcc with increasing film thickness. Similar observations have been reported in a scanning tunneling microscopy (STM) study of Hahn et al. [13] for the Cu vacuum deposition on Pd(100) substrates. In this case the copper films were found to grow layer-by-layer with a sharp structural transition from an fcc phase to a pseudomorphic bct phase ($a=2.75$ Å, $c=3.10$ Å) with increasing film thickness. The phase transition is driven by the total strain energy of the copper film and the critical film thickness depends on the temperature.

The electrochemical deposition of copper on Ag(100) from sulfuric acid solutions was studied by Dietterle et al. [14] with in situ STM. They found a layer-by-layer growth of pseudomorphic copper up to 8 ML. The crystallographic structure of this film was shown to be bcc-like. With the deposition of the ninth layer the film structure changes and a wavy copper phase appears. Bittner et al. [15] reported a similar growth mechanism for the deposition of Cu onto Pt(100) from sulfuric acid solutions. The first five to 10 copper monolayers were found to grow pseudomorphically onto Pt(100), forming a bct phase. At higher thicknesses the copper relaxes to its bulk structure and a square-shaped moiré pattern is formed.

In this paper we present results from a combined in situ STM and in situ surface X-ray scattering (SXS) study of the initial stages of electrochemical copper deposition on Au(100) substrates. The growth of the bulk copper follows a rather complicated path, and STM measurements reveal that at least four different phases occur during film growth [16]. For film thicknesses ranging from the first pseudomorphic copper monolayer on gold, formed at underpotentials, up to 10 ML, we found with STM the growth of pseudomorphic copper. A bilayer of copper is formed on top of the underpotentially deposited copper monolayer and further growth of bulk copper proceeds in a layer-by-layer fashion. With in situ X-ray reflectivity measurements the unit cell parameters of the copper film were measured with high accuracy, and they turned out to be very close to the bcc structure. The Au(100) substrate obviously acts, due to an almost perfect lattice match, as a template for the growth of bcc copper, and the lower strain favors a layer-

by-layer growth over three-dimensional cluster growth. In addition, alloy formation has been inferred from the STM and SXS measurements.

2. Experimental

The STM measurements were performed with a TopoMetrix TMX 2010 microscope where the tip and sample potentials were controlled independently with a bipotentiostat. Tunneling tips were made from a tungsten wire (0.25 mm diameter) by etching in 2 M NaOH using standard procedures [17]. The tips were coated with Apiezon wax except for the apex in order to minimize the faradaic currents below the 0.1 nA range, whereas typical tunneling currents were 1–5 nA. A copper wire contained in a fritted glass tube served as a reference electrode. All images were obtained in the constant-current mode and are represented either as gray-scale images (white denotes the highest and black the lowest point of the image) or as shaded pictures (the surface appears as if illuminated from the left side). No digital filtering was employed. For both the X-ray and STM measurements a platinum wire was used as counter electrode. The electrolytes, 0.05 M H_2SO_4 + x mM Cu^{2+} ($0.1 \leq x \leq 1$), were prepared from 96% H_2SO_4 (Suprapur, Merck), $CuSO_4$ (p.a., Merck) and Milli-Q water.

The X-ray scattering experiments were performed at beam line X22A of the National Synchrotron Light Source at Brookhaven National Laboratory. The measurements were performed with focused monochromatic radiation with a wavelength $\lambda = 1.20$ Å. The cross-section of the incident beam at the sample was kept smaller than the 10 mm diameter Au(100) crystal face which was aligned along the (001) direction to better than 0.2°. Fixed detector slits (3 mm wide and 4 mm high) were placed 600 mm away from the sample. This provides a θ resolution of 0.2° full-width at half-maximum (FWHM), which was sufficiently broader than the sample mosaic of 0.05° FWHM. Thus, the reflected signal was integrated at a fixed sample orientation without carrying out the usual θ scan.

For convenience, a bct coordinate system was utilized to describe the reciprocal space vector, $\boldsymbol{Q} = (a^*, b^*, c^*)(h, k, L)$ rather than the usual face-centered coordinates. Here $a^* = b^* = 4\pi/\sqrt{2}a$, $c^* = 2\pi/a$, $a = 2.885$ Å, where L is along the surface normal direction. Bragg peaks are found when $h + k + L$ is even, e.g. at (002), (101), (011), (103). Scattering measurements were carried out along (00L) and (10L). To eliminate the diffuse background, the spectrometer was displaced along h by 0.03 reciprocal lattice units and the intensity at this position served as a base line, which was subtracted from the on-axis signal.

The electrochemical cell for in situ SXS experiments was designed to operate in both, the thin and thick layer geometries. A 4 μm thick plastic foil functioned as an X-ray window. In the thin layer configuration the electrolyte layer was about 0.01 mm thick. To improve the current distribution during the electrodeposition process, the cell was inflated, which produces a thick (5–10 mm thick) electrolyte layer. After electrodeposition the cell was deflated to the thin layer geometry. For the SXS measurements a solution of 1 mM $CuSO_4$ in 0.1 M H_2SO_4 was used. Although potentials were measured against a Ag/AgCl microelectrode, all potentials are given with respect to SCE.

The copper deposits in the X-ray scattering cell were prepared by first inflating the cell with electrolyte and then stepping the potential from the underpotential deposition (UPD) region (240 mV) to the overpotential deposition (OPD) region (−260 mV) for a period between 2 and 30 s. Immediately after the Cu deposition the potential was set to 0 mV during a 10 to 20 s time period necessary to drain the electrolyte and to switch to the thin layer configuration.

At 0 mV the deposit is metastable in the thick layer geometry since neither deposition nor dissolution is rapid. In the thin layer configuration, however, the copper films were not stable at this potential and the copper electromigrated from the middle of the crystal face to form a ring of copper deposit close to the perimeter of the crystal. This electromigration occurs because of a lateral potential drop in the thin layer geometry, and this causes dissolution in the center of the cell where the electrode potential is slightly greater than the

Nernst potential. To minimize this effect, the sample potential was held at −260 mV during the thin layer mode. Under these conditions additional Cu bulk deposition is marginal, because practically no Cu^{2+} ions are available in the thin electrolyte layer.

The Au(100) crystals were flame annealed for 10 min in a Bunsen burner flame at faint orange color [18] and then cooled to room temperature in air or under nitrogen. The flame annealing leads to a reconstructed Au(100) surface, but this reconstruction is lifted by the adsorption of sulfate or the deposition of Cu [19]. Due to the 25% excess of surface gold atoms in the reconstructed phase, lifting of the reconstruction leads to a (1×1) gold surface with a large number of small gold islands [19]. In order to prepare a Au(100) surface with a lower defect density for the X-ray measurements, they were electrochemically 'annealed' for 5 min at 600 mV vs. SCE in 0.05 M H_2SO_4 + 1 mM HCl. The addition of chloride ions enhances the gold mobility and accelerates the Ostwald ripening of the islands [20]. As revealed by STM, this procedure yields large terraces.

3. Specular reflectivity and truncation rods

The truncation of a surface gives rise to streaks of weak scattering which connect neighboring Bragg peaks with the same in-plane (h, k) component [21,22]. This weak scattering, referred to in the literature as specular reflectivity ($h=k=0$) or truncation rods (h, k = non-zero integers), is sensitive to the structure of substrate and deposit. SXS has been successfully used to determine the structure of many different surfaces, under vacuum [23] and electrochemical [24,25] conditions, and for buried interfaces [26]. The same mathematical form, $R(h, k, L)$, is used to express both the specular reflectivity and the truncation rods, and for simplicity we will refer to both as 'reflectivity'. In the kinematical approximation, $R(h, k, L)$ is simply related to the sum over atomic layers with the appropriate atomic form and phase factors for each layer.

The reflectivity from an ideally terminated Au(100) surface, far from the critical angle where the signal is enhanced, is given by [27–29]

$$R_{\mathrm{Au}}(h,k,L)=\left(\frac{2r_0}{cL}\right)^2\times|s_{\mathrm{Au}}(h,k,L)|^2 \tag{1}$$

where r_0 is the Thomson radius of the electron. The gold scattering factor is given by a semi-infinite sum over crystalline planes

$$s_{\mathrm{Au}}(h,k,L)=\mathrm{e}^{-W_{\mathrm{Au}}(\boldsymbol{q})}F_{\mathrm{Au}}(\boldsymbol{q})\times\sum_{n=-\infty}^{0}\mathrm{e}^{\mathrm{i}\pi n(h+k+L)} \tag{2}$$

where the atomic form factor for gold is given by $F_{\mathrm{Au}}(\boldsymbol{q})$, the Debye–Waller factor for gold is given by $W_{\mathrm{Au}}(\boldsymbol{q})$, and h and k are integers.

To describe the properties of a thin copper overlayer on Au(100), a model has been employed which includes the sum over a finite number of copper layers, s_{Cu}. For j copper layers which are epitaxial (and pseudomorphic) with the gold, the copper scattering factor is given by

$$s^j_{\mathrm{Cu}}(h,k,L)=F_{\mathrm{Cu}}(\boldsymbol{q})\,\mathrm{e}^{-W_{\mathrm{Cu}}(\boldsymbol{q})}\,\mathrm{e}^{\mathrm{i}\pi(h+k+Lr_{\mathrm{Au-Cu}})}\times\sum_{n=1}^{j}\mathrm{e}^{\mathrm{i}\pi n(h+k+Lr_{\mathrm{Cu-Cu}})} \tag{3}$$

where the spacing between the last gold layer and the first copper layer is $d_{\mathrm{Au-Cu}}=r_{\mathrm{Au-Cu}}(c/2)$ and the spacing between the copper layers is given by $d_{\mathrm{Cu-Cu}}=r_{\mathrm{Cu-Cu}}(c/2)$ and c denotes the gold lattice constant normal to the surface. $F_{\mathrm{Cu}}(\boldsymbol{q})$ and $W_{\mathrm{Cu}}(\boldsymbol{q})$ are the atomic form factor and Debye–Waller factor for copper. We mention in passing that this form of the scattering factor gives rise to quasi-Bragg peaks and Kiessig fringes. To eliminate these fringes (not observed) we incorporate a copper thickness distribution, where $P(j)$ is the probability that a point on the surface has j copper layers. The final form of the reflectivity is given by

$$R_{\mathrm{Cu-Au}}(h,k,L)=\left(\frac{2r_0}{cL}\right)^2\times\sum_{j=1}^{\infty}P(j)\times|s_{\mathrm{Au}}(h,k,L)+s^j_{\mathrm{Cu}}(h,k,L)|^2 \tag{4}$$

where the scattering factors from the semi-infinite gold sum, the top gold layer and the finite sum over the copper layers have been included. The

copper thickness distribution is modeled via a Gaussian form

$$P(j)=\frac{e^{-(j-N_{Cu})^2/\Delta^2}}{\sum_{j=1}^{\infty} e^{-(j-N_{Cu})^2/\Delta^2}} \quad (5)$$

where the peak in the distribution function is at N_{Cu} and the width is Δ. The average thickness, for practical purposes, is very close to the function's peak value. We have used the form of the reflectivity given by Eq. (4) in the analysis of the data presented in the next section.

To demonstrate the essential features of the model, calculated specular reflectivity curves are shown in Fig. 1 for three different sets of parameters. The strong scattering near $L=2$ is from the (002) Bragg reflection and is nearly independent of the copper coverage. The ideal curve, shown as the dotted line, falls off monotonically between the Bragg peaks. For the other two curves, both corresponding to eight copper layers, a well-defined quasi-Bragg peak is found at $L=2.8$. For a homogeneous film (dashed curve) subsidiary maxima and minima (Kiessig fringes) are also observed. For an inhomogeneous film with $\Delta=2.5$ (solid line) these additional fringes are greatly reduced.

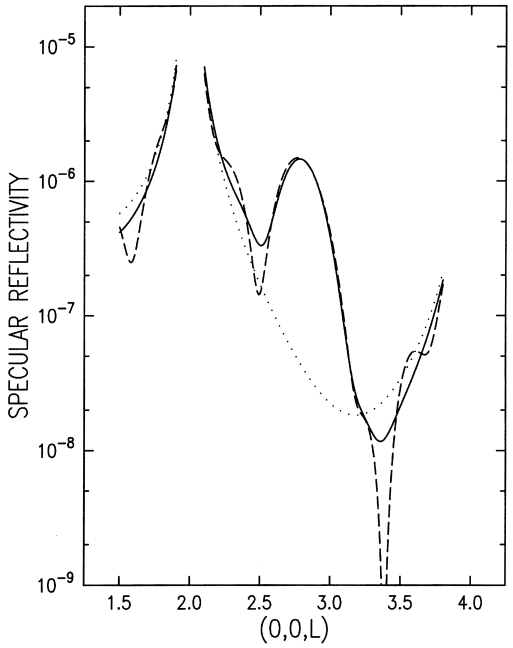

Fig. 1. Calculated X-ray specular reflectivity curves according to the model given in the text: ideal, copper-free Au(100) surface (dotted); with a homogeneous, eight-layer thick copper film (dashed) and with an inhomogeneous eight-layer copper film with $\Delta=2.5$ (solid line).

4. Results and discussion

Electrodeposition of copper on a Au(100) surface starts with the formation of a monolayer at potentials positive of the Nernst potential [30]. This so-called UPD results from a copper–gold interaction which exceeds that between copper and copper. Bulk copper is deposited at OPD, i.e. at potentials negative of the Nernst potential. In the following we report morphological and atomic structure measurements on thin copper films (less than 10 copper layers) obtained from in situ STM and SXS experiments. Our findings show that within this thickness regime the copper films exhibit a stable bcc phase. Both the X-ray reflectivity and the STM measurements suggest that a copper–gold alloy is gradually formed at the interface.

4.1. Cyclic voltammetry

The cyclic voltammogram for the copper deposition onto Au(100) in 0.05 M H_2SO_4 + 1 mM $CuSO_4$ is shown in Fig. 2. Bulk copper deposition occurs at potentials less than 0 mV. At more positive potentials, in the region between 100 mV and 350 mV, copper monolayer formation (negative current) and dissolution (positive current) take place, and give rise to two pronounced current peaks. For the sake of clarity, the range between 50 and 500 mV has been enlarged by a factor of 10 and is shown by the dashed curve. Below 170 mV copper forms a complete (1×1) monolayer on top of the gold substrate [30]. The charge under the UPD peaks is about 400 $\mu C/cm^2$, which is the expected value for a monolayer from divalent cations. At more negative potentials, below -20 mV, bulk copper deposition starts and this gives rise to a large cathodic current. Scanning in the positive direction, dissolution of the deposited copper is seen in a large anodic

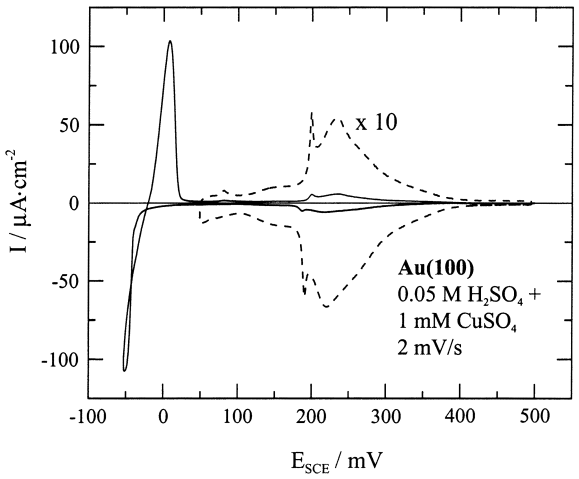

Fig. 2. Cyclic voltammogram of Au(100) in 0.05 M H_2SO_4 + 1 mM $CuSO_4$ showing copper deposition in the under- and overpotential region. Sweep rate: 2 mV/s.

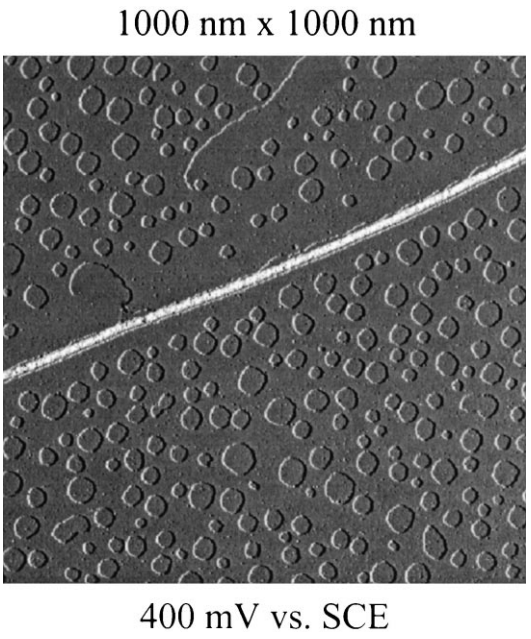

Fig. 3. STM image (shaded) of a bare Au(100) surface in 0.05 M H_2SO_4 + 1 mM $CuSO_4$ at 400 mV vs. SCE. The surface exhibits a small region of step bunching (bright stripe across the image), two screw dislocations and numerous monoatomic high gold islands, which cover about 25% of the substrate surface.

current peak. In Fig. 2 this charge amounts to 2450 μC/cm^2, corresponding to the equivalent of six layers of pseudomorphic copper.

4.2. *In situ STM*

STM measurements were carried out to investigate the structure and morphology of electrodeposited copper films on Au(100). We note that the morphology of the copper film is greatly influenced by that of the underlying Au(100) surface. A typical STM image (differentiated representation) of the bare Au(100) surface at 400 mV is shown in Fig. 3. In addition to step edges and screw dislocations, which are common defects on single crystal surfaces, the Au(100) surface exhibits a large number of gold islands, because it was not electrochemically annealed. Their step height of 2.0 Å corresponds to a single Au(100) layer. These islands are formed during lifting of the hex-reconstruction by the excess gold atoms that are expelled in order to form the less dense (1×1)-terminated surface [19]. The size distribution of the islands is characteristic of an Ostwald ripening process; the bigger islands increase in size with time, while the smaller ones disappear [18].

Fig. 4 shows the initial stages of the overpotential copper deposition on top of the UPD monolayer. This surface exhibits a few monoatomic high gold islands. At the applied potential of -250 mV nucleation of the bulk copper phase is seen to start at the rims of the gold islands. Copper nucleation on flat terraces is rarely observed. This demonstrates the importance of surface defects as the principal nucleation sites for the metal deposition reaction. Similar effects have also been observed for copper deposition on Au(111) [31]. In the earliest stages of electrodeposition the copper forms rims around the gold islands which are higher than the island plateaus (see Fig. 4a). Cross-sections through the surface (see example in Fig. 4b) show that the copper crystallites have a height of 2 ML (0.30 ± 0.01 nm) in addition to the copper UPD layer. This copper bilayer grows from the nucleation site onto the terrace, usually in rectangular-shaped patches, demonstrating the influence of the substrate symmetry. The two copper monolayers, which surround the rims of the gold islands, form a new step-like edge (its

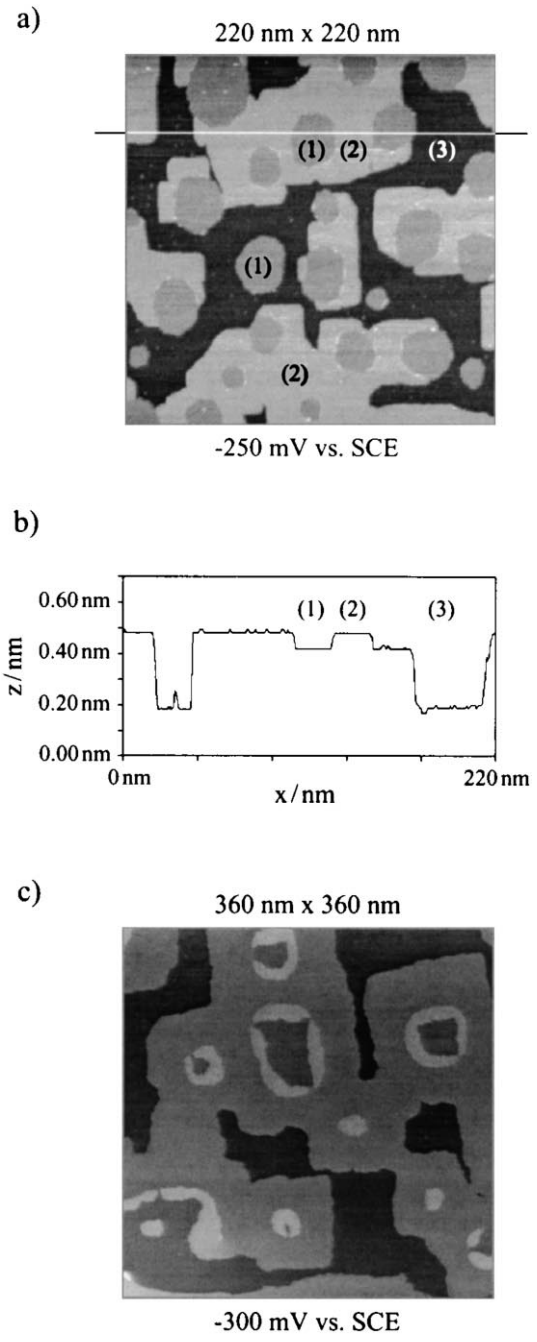

Fig. 4. (a) STM gray-scale image of the initial stages of copper deposition onto Au(100) in 0.05 M H_2SO_4 + 0.5 mM $CuSO_4$ at −250 mV vs. SCE. The gold surface is covered by a Cu UPD layer. Copper nucleates at the rims of the gold islands (1) by forming a bilayer (2). (b) Cross-section along the marked line in (a), demonstrating the growth of a copper bilayer at the rims (step edges) of the gold islands. (c) STM gray-scale image of the copper growth on top of the Au islands in 0.05 M H_2SO_4 + 0.5 mM $CuSO_4$ at −300 mV vs. SCE. The copper bilayer is slightly higher than a monoatomic gold step and hence provides nucleation centers for copper deposition on top of the islands. Starting from the island rims, the copper grows again as a bilayer towards the centers of the islands.

height being only a fraction of a normal step height), which acts as a nucleation site for copper deposition onto the top of the islands (see Fig. 4c). The critical height of a bcc copper nucleus on Au(100) was always 2 ML (three including the UPD layer) and stable nuclei with heights of 1 ML only (two including the UPD layer) were never observed.

Beyond the first three copper layers on Au(100), further growth proceeded in a layer-by-layer fashion, the new copper layers almost exclusively starting to grow at defects; nucleation on flat terraces was rarely seen. We have observed the growth of 10 atomically flat monolayers (including the UPD layer) and atomically resolved images revealed that all of them grew pseudomorphically onto the gold substrate. This Frank–van der Merwe growth of a pseudomorphic copper phase is quite surprising, as the lattice constant of Cu (3.615 Å) is about 13% smaller than that of Au (4.080 Å). Hence, the pseudomorphic layers are under a large tensile (misfit) stress and a 10-layer thick film should not be stable. The misfit is so large that, according to the conventional picture of elastic distortions, layer-by-layer growth should not occur at all. The classical van der Merwe model predicts the creation of misfit dislocations for a film thicker than 1 ML with a further growth via three-dimensional clusters [9]. This is indeed observed for copper deposition on Au(111) surfaces [31].

Cross-sections (see example in Fig. 4b) through the copper layers (up to the first 10 layers) reveal a step height of 0.15 ± 0.1 nm instead of the expected 0.18 nm for fcc copper. This height, along with the pseudomorphic in-plane spacing, indicates that the structure of these copper films cannot be fcc. Layer spacing and in-plane lattice constant support the notion that the copper film is 'bcc-like'. The atomic spacing of the Au(100) surface, within 1%, ideally matches the lattice constant of bcc copper, which is predicted by a calculation

that assumes identical atomic volumes for both the fcc and bcc configurations. Although the bcc copper by itself is metastable, it appears to be stabilized by the underlying gold surface. The existence of a bcc copper phase is also supported by recent publications of copper deposition on Ag(100) [14] and Pt(100) [15] in an electrochemical environment and on Ag(100) and Pd(100) under UHV conditions [11–13], which show that (100) substrates can initiate the growth of bcc or bct copper phases. Further support comes from theoretical calculations, which predict that the bcc phase of copper is only about 20–38 meV less stable than the fcc phase [9,10,32].

With the deposition of the eleventh copper layer, a wavy surface morphology appears [16]. Separate X-ray scattering measurements indicate that this involves the restructuring of all the underlying copper layers [32] and not just the top layer of copper. Fig. 5a shows a STM image with regions which are 10 ML thick (pseudomorphic copper film) and with regions which are 11 ML thick (striped and buckled copper film). Positions where the underlying Au(100) substrate exhibits islands (see Fig. 3) are clearly visible on top of the copper film. Depending on the thickness of the copper film, these islands appear as bright or dark patches in the STM picture (see model in Fig. 5b). The 10-layer thick copper film appears atomically flat except at the rims of the copper islands which were formed on top of the underlying gold islands. Directly at the rims of the islands the film buckles (Fig. 5b) and this is obviously the precursor of the striped phase. This edge effect occurs along the principal in-plane directions, still below the critical height of 11 ML for the phase transformation. Clearly, the islands induce a higher strain in the film at the step edges and this reveals the influence of defects, not only on the phase formation (acting as nucleation centers) but also on phase transformations.

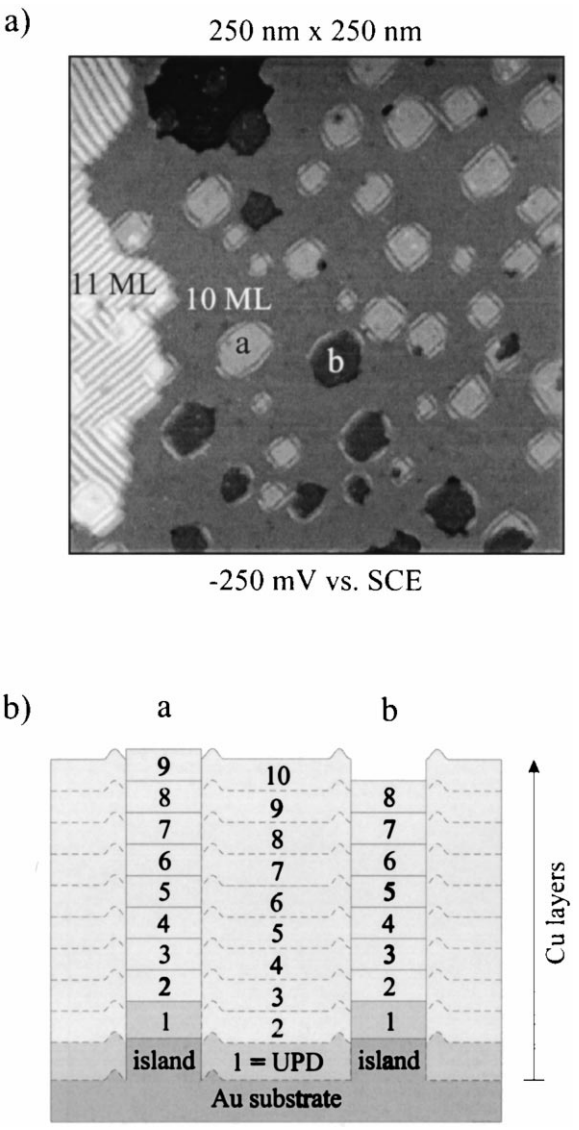

Fig. 5. (a) STM gray-scale image of a 10 ML thick copper film grown on Au(100) in 0.05 M H_2SO_4 + 0.5 mM $CuSO_4$ at −250 mV vs. SCE. Only a small fraction of the surface is covered with an 11-layer thick film which has a buckled structure. The 10-layer thick film appears flat, except at the rims of those islands which originate from the underlying substrate islands. (b) Sketch of a cross-section through the surface, demonstrating the different appearance of the islands a and b as a consequence of the different height of the copper film on top of the Au islands.

4.3. X-ray reflectivity and truncation rods

Here we report the results of X-ray scattering measurements in the intermediate coverage regime (less than 10 Cu layers). In addition, a search was carried out in reciprocal space for diffraction features different from those originating from the pseudomorphic copper layers. No new diffraction features were observed and this allows us to rule

out the presence of high-order incommensurate, uniaxially incommensurate, or hexagonal phases. The absence of diffraction at these other positions supports the STM observation that the copper layers are pseudomorphic with the underlying gold lattice. Specular reflectivity and the lowest order truncation rod (along L at fixed integral $h=1$ and $k=0$) are shown at several coverages in Fig. 6 and Fig. 8, respectively. The peaks at $L=2$ (Fig. 6) and $L=1$ (Fig. 8) result from the (002) and (101) Bragg peaks of the underlying Au(100) lattice. After sufficient copper deposition (discussed below), a broad peak emerges near $L=2.8$ in the specular reflectivity (Fig. 6, curves b–d) and concomitantly a shoulder develops near $L=1.4$ in the truncation rod (Fig. 8). The position of the copper peak observed in the specular profile ($L=2.8$) provides an approximate measure of the out-of-plane copper layer spacing, $2\pi/2.8c^*=2.90$ Å. This is very close to the in-plane lattice constant, 2.885 Å, and suggests the formation of a structure very close to bcc copper. Detailed fitting analysis of the profiles (presented below) provides a more accurate measure of the copper lattice constant, the gold–copper layer spacing, along with additional structural parameters.

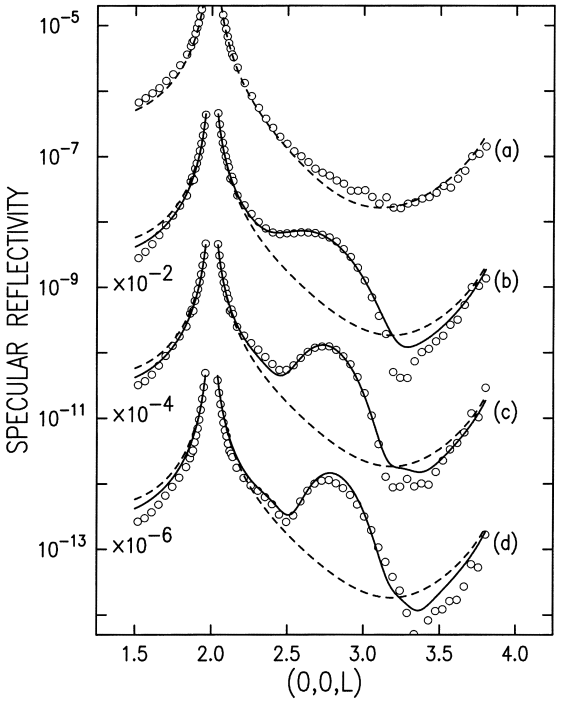

Fig. 6. X-ray reflectivity (0, 0, L) of the bare Au(100) surface at 500 mV (a) and after deposition of various amounts of Cu (b–d). The curves have been displaced by two decades for clarity. The quasi-Bragg peak at $L=2.8$ results from the bct copper film. The ideal reflectivity for the bare gold surface is shown as a dashed line and the fits (discussed in the text) are drawn as solid lines.

Fig. 6 shows the specular reflectivity for three different deposition conditions (b–d) along with data at 500 mV (a) where there is no copper on the gold surface. For the latter, the reflectivity resembles that of a nearly perfectly terminated gold lattice; a monotonic decrease in the intensity around the (002) Bragg peak and no additional features between the (002) and (004) Bragg peaks. After 10 s deposition at -260 mV (curve b), significant differences in the reflectivity emerge. A plateau develops at about $L=2.6$ followed by a sharp fall-off. For reflectivities obtained after longer deposition times this plateau transforms into a well-defined quasi-Bragg peak at $L=2.8$. This is demonstrated by the curves c and d which were obtained after multiple deposition cycles without prior stripping the copper. The total deposition times for curves c and d are 17 and 27 s, respectively. The finite width of the peak results from the small number of adsorbed layers. The absence of Kiessig fringes, which would be indicative of a film with uniform thickness, implies a significant variation in the number of deposited layers within the area sampled by the X-ray. We note that the specular curves have been normalized by a constant value. This constant was chosen such that the intensity close to the (002) peak, where the intensity is very insensitive to the details of the surface structure, agrees with the ideal, absolute reflectivity curve.

After sufficient deposition, the reflectivity curves no longer exhibit a single peak at $L=2.8$, but rather two peaks are observed at $L=2.62$ and 3.07 (not shown). Concomitantly, off-axis satellite peaks appear at either $(0, 0.05, 2.8\pm0.18)$, corresponding to a modulated phase. The structure of this modulated phase will be discussed elsewhere [32].

The specular reflectivities from the bare Au(100) surface and from the Au(100) surface

after copper electrodeposition have been analyzed according to Eqs. (1)–(4). The Debye–Waller displacements, σ_{Au} and σ_{Cu}, were fixed at 0.085 Å and 0.16 Å, respectively [33]. The reflectivity with no copper at 500 mV (a) is reasonably well described by an ideal Au(100) surface (dashed line). The same ideal reflectivity curve is shown for the data sets (b–d).

The reflectivities from the film-covered surfaces, shown in Fig. 6, were fitted to Eq. (4) where three parameters were allowed to vary; the number of copper layers (N_{Cu}), the normalized Cu–Cu layer spacing (r_{Cu-Cu}, see Eq. (3)), and the normalized Au–Cu layer spacing (r_{Au-Cu}). In the first round of fits the layer width, Δ, was also allowed to float, but the variation of this parameter with thickness was not significant. In all subsequent fits this parameter was constrained to its average value, $\Delta = 2.5$. The best fits, shown as solid lines in Fig. 6, describe very well all the essential features of the reflectivity curves, including the regions near the (002) peak and the copper quasi-Bragg peak. The number of copper layers, N_{Cu}, is equal to (b) 4.2, (c) 6.7, and (d) 7.9. Although an off-axis modulation peak (satellite spots) is observed for the 7.9-layer thick film (not shown here), the weak intensity implies that most of the surface is covered by the pseudomorphic phase. Given the large variation in thickness, $\Delta = 2.5$, thicker films should exhibit considerable coexistence between pseudomorphic and modulated phases, thus complicating their analysis. The large value of Δ implies that there is a variation in the copper thickness at different sample positions. This may be a consequence of potential gradients associated with the cell design.

The present model assumes that regions with the same film thickness are large compared with the coherence length of the spectrometer resolution (typically hundreds of angstroms), so that the scattering from regions of different film thicknesses adds incoherently. We have also considered a model where the scattering from regions with different copper heights adds coherently. Both models give the same average thickness (within 0.5 layers), and on the basis of the fit quality it is not possible to select one model over the other. The incoherent model is physically more appealing since the STM images indicate a domain size of several hundred angstroms which is larger than the effective spectrometer resolution. Diffuse scattering measurements, in principle, could help identify the facet distribution and the appropriateness of the present model. However, the large contribution to the diffuse scattering from the plastic membrane and from the electrolyte limits the resolving power of these measurements.

In Fig. 7 the layer spacing, obtained from the fits (see Fig. 6), is shown as a function of the film thickness N_{Cu}. The solid line is the expected layer spacing for bcc copper and the dashed line represents the underlying gold layer spacing. The copper–copper layer spacing (open circles) decreases from 1.46 to 1.43 Å with increasing thickness. This thickness variation straddles the value expected for a cubic unit cell, 1.443 Å, shown as the solid line in Fig. 7, and is in good agreement with the 1.5 ± 0.1 Å thickness obtained by our STM measurements. Furthermore, the volume per copper atom ($1.45\ \text{Å} \times 2.885^2\ \text{Å}^2 = 12.1\ \text{Å}^3$) is only moderately larger than the corresponding bulk copper value, 11.8 Å^3. The product of the junction spacing (between the first copper layer and the top gold layer) and Q_z (component of the scattering vector normal to the surface) gives rise to a phase

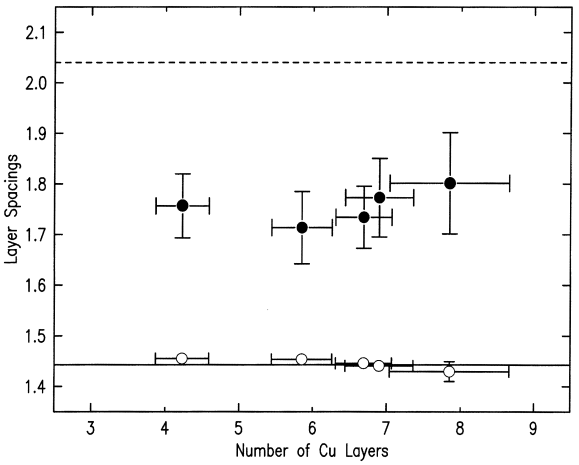

Fig. 7. Copper layer spacing (open circles) and gold–copper spacing (filled circles) as a function of film thickness derived from an analysis of the reflectivity curves in Fig. 6 (curves b–d). The solid line is the expected layer spacing for bcc copper. The dashed line is the Au(100) layer spacing.

factor whose value affects the symmetry in the wings of the copper quasi-Bragg peak at $L=2.8$. The fits are sensitive to this symmetry and thus provide an accurate measure of the gold–copper layer spacing. The average Au–Cu spacing (filled circles) obtained from the fits, 1.74 ± 0.10 Å, is very close to the expected 1.74 Å layer spacing obtained by averaging the gold fcc and copper bcc lattice constants.

The truncation rod scattering (along L with non-zero, integer h and k) is sensitive to the crystalline order of the copper film and to the epitaxial relationship of the film with the underlying gold substrate [21,22]. In Fig. 8 we show truncation rod data, (1, 0, L), for the 'pure' substrate with no copper (500 mV) as open circles and after depositing copper for 10 s as filled circles. The scattering very close to the (1, 0, 1) Bragg peak is nearly independent of the deposition conditions. Further in the wings, the weak scattering depends greatly on the deposition conditions. With increasing copper coverage, the asymmetry around the (1, 0, 1) peak increases; at lower L the intensity decreases and at higher L the intensity increases.

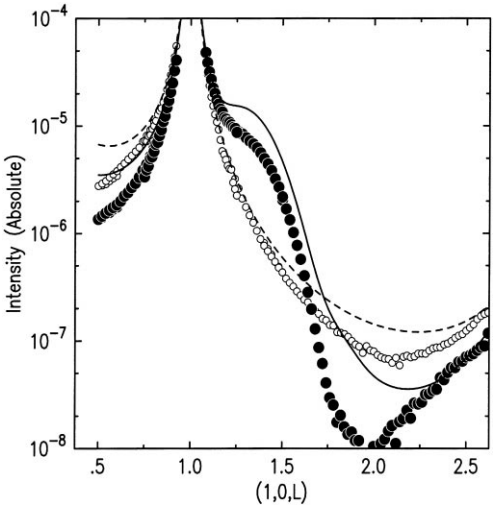

Fig. 8. X-ray truncation rod (1, 0, L) for the bare Au(100) surface at 500 mV (open circles) and for Au(100) after electrodepositing copper for 20 s (filled circles). The shoulder at $L=$ 1.4 results from the deposition of copper. The ideal reflectivity is given as a dashed line, while the solid line has been obtained by using the parameter set derived from the specular data (Fig. 5, curve c).

In addition, there is a shoulder between $L=1.2$ and 1.5, followed by a sharp fall-off. In contrast to the specular direction, where a clearly defined copper peak is evident, a well-defined copper peak never emerges in the truncation rod. We note that the numerical factor used to normalize the specular reflectivity correctly normalizes the (1, 0, L) truncation rod scattering near the (1, 0, 1) peak. This agreement strengthens our confidence in the data presented.

The existence of a well-defined copper peak depends on the proximity to a substrate Bragg peak. The copper peaks, for a sufficiently thick film, are expected at values of L which are about a factor of 1.4 larger than those from the substrate. Therefore, the copper peak corresponding to the gold (1, 0, 1) peak should be at (1, 0, 1.4). Since the L peak widths are always the same, for the same number of layers, the peak at (1, 0, 1.4) is masked by the nearby Bragg peak at (1, 0, 1). A dip in the reflectivity might be expected at (1, 0, 1.1) on the basis of the position of the dips in the reflectivity measurements. However, when the strong scattering from the gold is considered, the expected dip vanishes in the measured reflectivity.

In Fig. 8 the truncation rod data are compared with the scattering model associated with Eq. (4). The ideal reflectivity curve, shown as a dashed curve, is always higher than the corresponding data (open circles) but exhibits the same overall shape. For both data sets, below $L=0.8$ the measured intensity is less than the calculated intensity, and this discrepancy results from resolution volume artifacts which have not been included.

Rather than fitting the truncation rod data to the model, in Fig. 8 we compare the calculated truncation rod profile (solid line) using the parameters from curve c in Fig. 6 ($N_{Cu}=6.7$) with the truncation rod data (solid circles). The model truncation rod curve exhibits the same overall shape as the data, including the plateau between $L=1.1$ and 1.5, and in this region there is a significant increase (by nearly a factor of 10) in the scattered intensity compared with the 'bare' surface. In addition, the in-plane diffraction widths are independent of coverage at all L. Together, these facts indicate that the copper film is pseudo-

morphic and this rules out the existence of an incommensurate phase. We note that on the basis of the specular reflectivity alone this determination could not be made. Finally, the discrepancy in the intensity, especially near $L=1.4$, results from an overestimation of the contribution from the copper scattering in the model. This might result from regions with no copper or an enhanced rms Debye–Waller-like amplitude. The latter may result from a reduction of the elastic constants (soft mode) which precedes the formation of the buckled phase [32].

4.4. Interfacial alloying

The stress at the interface between two different metals can be partially relieved by the formation of an alloy. However, direct structural information from such buried phase boundaries is scarce. In the bulk, copper and gold are miscible, therefore alloy formation at the interface between gold substrate and copper overgrowth is likely. Both the X-ray scattering and STM measurements provide evidence for alloy formation.

In the X-ray measurements, the results depend on the history of the electrochemical treatment, and we attribute this to alloy formation. For instance, the reflectivity profiles for a given deposition time are not the same. Our findings show that after repeated deposition/dissolution cycles, the copper features in the reflectivity are not as pronounced as after one cycle with correspondingly longer deposition time. In addition, the reflectivity profiles change with time, and small effects are apparent after several hours of data collection; this might be attributed to interfacial alloying.

With STM it is impossible to probe directly buried interfaces. However, the morphology of the interface can be probed after dissolving the copper film, because the existence of an alloy should change the morphology of the gold substrate [18]. For such measurements thick copper films (>10 ML) were prepared, and after a waiting period of 20 min the copper was dissolved. At dissolution potentials positive of the UPD region, the surface structure changes rapidly with time due to the so-called electrochemical annealing [18,20], and it is difficult to obtain quantitative information. At a potential of 100 mV, i.e. in the UPD regime where a full copper monolayer is on the surface, bulk copper and the copper of the interfacial alloy dissolve, whereas the morphology of the gold surface remains unchanged, and hence small surface structures, like small islands and holes (vacancy clusters) can easily be detected by STM [30].

The gold surface shown in Fig. 9, which was obtained after deposition and dissolution of a copper film, is much rougher than the freshly prepared Au(100) surface shown in Fig. 3. This rough surface is composed of monoatomic high gold islands and monoatomic deep holes with sizes extending over a relatively large range of length scales. On top of the larger islands additional smaller islands are seen, and on the bottom of the larger holes smaller holes are visible. The changes in the gold surface morphology originate from the dissolution of an interfacial alloy [18]. This rough-

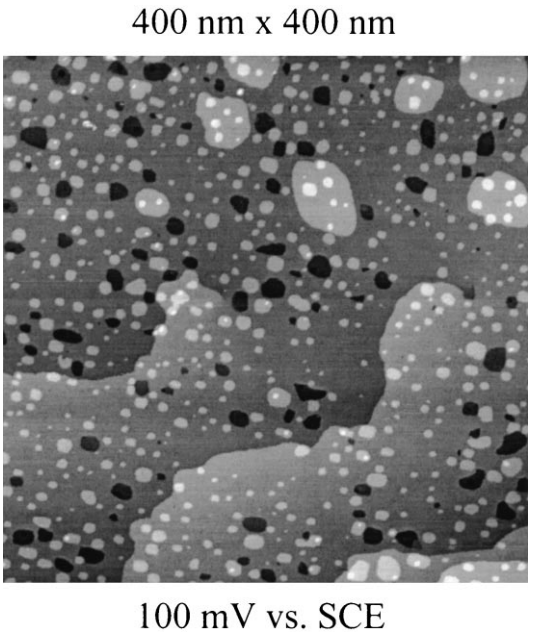

Fig. 9. STM gray-scale image of a Au(100) surface in 0.05 M H_2SO_4+1 mM $CuSO_4$ at 100 mV vs. SCE after dissolution of a thick copper film. The surface appears disordered and is covered with holes and islands which originate from the dissolution of an interfacial alloy.

ening process also explains why the sample history affects the X-ray results.

5. Summary

We have investigated copper bulk deposition on Au(100) electrodes from sulfuric acid solutions with in situ STM and in situ SXS. Our results concerning film growth and film structure can be summarized as follows.

1. Nucleation of the copper bulk phase, which is deposited on top of the performed UPD monolayer, starts at surface defects of the Au(100) substrate. The critical height of the (usually square-shaped) copper nuclei is 2 ML (3 ML including the UPD layer).
2. The further growth of the copper film proceeds in a layer-by-layer fashion, as shown by STM. The next layer often starts to grow before the underlying copper layer is completed (pseudo-layer-by-layer growth); this leads to macroscopically rough films with a thickness distribution which increases with film height.
3. Up to a thickness of 10 ML, the film consists of atomically flat terraces separated by monoatomic high copper steps. Both techniques show that the in-plane structure of the copper film is pseudomorphic with the Au(100) substrate ($a=b=2.885$ Å). Analysis of the reflectivity gives $c=2.89\pm0.03$ Å which is close to twice the 1.5 Å layer spacing measured with STM. Therefore the film structure is, besides a small tetragonal distortion, very close to bcc.
4. The layer spacing between the top gold layer and the first copper layer is 1.74 ± 0.10 Å. This is very close to the expected 1.74 Å layer spacing obtained by averaging the gold fcc and copper bcc lattice constants.
5. The variation of the film thickness across the sample can be modelled by a Gaussian profile with a full width of 2.5 layers.
6. At the interface between Au(100) substrate and copper film a 2–4 ML thick Cu/Au alloy is formed within a time span of about 20 min.
7. Deposition of the eleventh copper layer changes the film structure and a buckled/modulated structure appears [16,32].

Acknowledgements

The authors would like to thank J.X. Wang and R.R. Adžić for their help and stimulating discussions. One of us (R.R.) gratefully acknowledges financial support by the Landesgraduiertenförderung von Baden-Württemberg. BNL and the University of Illinois are supported by DOE Grants DE-AC-02-98CH10886 and DE-FG-02-96-ER45439, respectively. This work was supported by the Deutsche Forschungsgemeinschaft through Graduiertenkolleg No. 328 'Molekulare Organisation und Dynamik an Grenz- und Oberflächen'.

References

[1] E. Budevski, G. Staikov, W.J. Lorenz, Electrochemical Phase Formation and Growth: An Introduction to the Initial Stages of Metal Deposition, VCH, Weinheim, 1996.
[2] D.M. Kolb, in: Schering Lectures Publication Vol. 2, Schering Research Foundation, Berlin, 1991, p. 1.
[3] C. Günther, S. Günther, E. Kopatzki, R.Q. Hwang, J. Schröder, J. Vrijmoeth, R.J. Behm, Ber. Bunsenges. Phys. Chem. 97 (1993) 522.
[4] E. Bauer, J.H. van der Merwe, Phys. Rev. B 33 (1986) 3657.
[5] F.C. Frank, J.H. van der Merwe, Proc. Roy. Soc. London, Ser. A 198 (1949) 205.
[6] R. Bruinsma, A. Zangwill, J. Phys. 47 (1986) 2055.
[7] W. Wormester, E. Hüger, E. Bauer, Phys. Rev. Lett. 77 (1996) 1540.
[8] A.T. Paxton, M. Methfessel, H.M. Polatoglou, Phys. Rev. B 41 (1990) 8127.
[9] J.R. Chelikowsky, M.Y. Chou, Phys. Rev. B 38 (1988) 7966.
[10] T. Kraft, P.M. Marcus, M. Methfessel, M. Scheffler, Phys. Rev. B 48 (1993) 5886.
[11] W.F. Egelhoff, I. Jacob, J.M. Rudd, J.F. Cochran, B. Heinrich, J. Vac. Sci. Technol. A 8 (1990) 1582.
[12] D.T. Jiang, E.D. Crosier, B. Heinrich, Phys. Rev. B 44 (1991) 6401.
[13] E. Hahn, E. Kampshoff, N. Wälchli, K. Kern, Phys. Rev. Lett. 74 (1995) 1803.
[14] M. Dietterle, T. Will, D.M. Kolb, Surf. Sci. 396 (1998) 189.
[15] A.M. Bittner, J. Wintterlin, G. Ertl, Surf. Sci. 376 (1997) 267.
[16] R. Randler, M. Dietterle, D.M. Kolb, Z. Phys. Chem. 208 (1999) 43.
[17] D.M. Kolb, R.J. Nichols, R.J. Behm, in: R. Guidelli (Ed.), Electrified Interfaces in Physics, Chemistry and Biology, NATO ASI Series C Vol. 355, Kluwer Academic, Dordrecht, 1992, p. 275.

[18] A.S. Dakkouri, M. Dietterle, D.M. Kolb, in: R. Helbig (Ed.), Feskörperprobleme/Advances in Solid State Physics Vol. 36, Vieweg, Braunschweig/Wiesbaden, 1996, p. 1.
[19] A.S. Dakkouri, Solid State Ion. 94 (1997) 99.
[20] J.L. Stickney, I. Villegas, C.B. Ehlers, J. Am. Chem. Soc. 111 (1989) 6473.
[21] I.K. Robinson, D.J. Tweet, Rep. Progr. Phys. 55 (1992) 599.
[22] R. Feidenhans'l, Surf. Sci. Rep. 10 (1989) 105.
[23] P. Eisenberger, W.C. Marra, Phys. Rev. Lett. 46 (1981) 1081.
[24] M.F. Toney, in: C.A. Melendres, A. Tadjeddine (Eds.), Synchrotron Techniques in Interfacial Electrochemistry, NATO ASI Series C Vol. 432, Kluwer Academic, Dordrecht, 1994.
[25] J.X. Wang, N.S. Marinković, R.R. Adžić, B.M. Ocko, Surf. Sci. 398 (1998) L291.
[26] I.K. Robinson, W.K. Waskiewicz, R.T. Tung, Phys. Rev. Lett. 57 (1986) 2714.
[27] D. Gibbs, B.M. Ocko, D.M. Zehner, S.G.J. Mochrie, Phys. Rev. B 38 (1988) 7303.
[28] S.G.J. Mochrie, D.M. Zehner, B.M. Ocko, D. Gibbs, Phys. Rev. Lett. 64 (1990) 2925.
[29] B.M. Ocko, D. Gibbs, K.G. Huang, D.M. Zehner, S.G.J. Mochrie, Phys. Rev. B 44 (1991) 6429.
[30] F.A. Möller, O.M. Magnussen, R.J. Behm, Phys. Rev. B 51 (1995) 2484.
[31] T. Will, M. Dietterle, D.M. Kolb, in: A.A. Gewirth, H. Siegenthaler (Eds.), Nanoscale Probes of the Solid/Liquid Interface, NATO ASI Series E Vol. 288, Kluwer Academic, Dordrecht, 1995, p. 137.
[32] B.M. Ocko, I.K. Robinson, M. Weinert, R. Randler, D.M. Kolb, Phys. Rev. Lett. 83 (1999) 780.
[33] E. Vlieg, I.K. Robinson, R. McGrath, Phys. Rev. B 41 (1990) 7896.